

# Mesoporous Ultrathin $\text{In}_2\text{O}_3$ Nanosheet Cocatalysts on a Silicon Nanowire Photoanode for Efficient Photoelectrochemical Water Splitting

Guangyuan Yan,\* Yutao Dong, Tong Wu, Shuming Xing,\* and Xudong Wang\*

Cite This: *ACS Appl. Mater. Interfaces* 2021, 13, 52912–52920

Read Online

ACCESS |



Metrics &amp; More



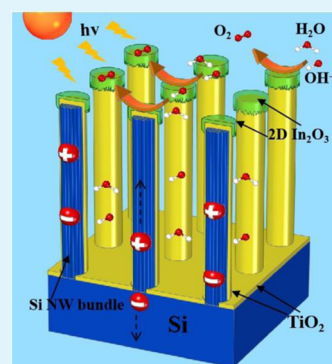
Article Recommendations



Supporting Information

**ABSTRACT:** Vertical Si nanowire (NW) arrays are a promising photoanode material in the photoelectrochemical (PEC) water splitting field because of their highly efficient light absorption capability and large surface areas for PEC reactions. However, Si NW arrays always suffer from high overpotential, low photocurrent density, and low applied bias photon-to-current efficiency (ABPE) due to their low surface catalytic activity and intense charge recombination. Here, we report an efficient oxygen evolution cocatalyst of optically transparent, mesoporous ultrathin (2.47 nm thick)  $\text{In}_2\text{O}_3$  nanosheets, which are coupled on the top of Si NW arrays. Combined with a conformal  $\text{TiO}_2$  thin film as an intermediate protective layer, this Si NW/ $\text{TiO}_2$ / $\text{In}_2\text{O}_3$  (2.47 nm) heterostructured photoanode exhibited an extremely low onset potential of 0.6 V vs reversible hydrogen electrode (RHE). The Si NW/ $\text{TiO}_2$ / $\text{In}_2\text{O}_3$  (2.47 nm) photoanode also showed a high photocurrent density of  $27 \text{ mA cm}^{-2}$  at 1.23 V vs RHE, more than 1 order of magnitude higher than that of the Si NW/ $\text{TiO}_2$  photoanodes. This improvement in solar water splitting performance was attributed to the significantly promoted charge injection efficiency as a result of the  $\text{In}_2\text{O}_3$  nanosheet coupling. This work presents a promising pathway for developing efficient Si-based photoanodes by coupling ultrathin 2D cocatalysts.

**KEYWORDS:** photoelectrochemical water splitting, Si photoanode, two-dimensional nanomaterials, cocatalyst, ionic layer epitaxy



## INTRODUCTION

As one of the most promising methods to produce solar fuel, photoelectrochemical (PEC) water splitting can be capable of directly converting solar energy into clean and sustainable hydrogen fuel.<sup>1–6</sup> To achieve these goals, it is essential to select efficient, robust, and inexpensive photoanode materials.<sup>7</sup> As an ideal photoanode material, silicon (Si) has become a viable commercial PEC electrode material due to its optimal energy band structure, abundant earth reserves, good charge transport properties, and mature production technologies.<sup>7,8</sup> Compared to planar Si, vertical Si nanowire (NW) arrays show improved PEC performance due to enhanced light absorption by their increased transmission path of light, promoted carriers transport by its axial one-dimensional (1D) conducting channels, and improved electrode/electrolyte interfacial electrochemical reactions by enlarged surface active areas.<sup>8,9</sup> However, these Si NW arrays typically exhibit low surface catalytic activity, undesirable charge recombination, and fast surface corrosion/passivation in PEC reactions, which seriously impair their overpotential, photocurrent density, and stability.<sup>8,10</sup> The stability of Si NW arrays can be improved by coating their surface by  $\text{TiO}_2$  thin films through atomic layer deposition (ALD) because the presence of a  $\text{TiO}_2$  thin film would cause the surface of Si NW arrays to be completely isolated from the alkaline electrolyte, but the Si NW/ $\text{TiO}_2$  composite structure still suffers from a high overpotential and

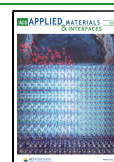
low photocurrent density as well as low applied bias photon-to-current efficiency (ABPE).<sup>8,11,12</sup>

Introducing cocatalysts to photoanodes can effectively reduce the overpotential and promote the charge transfer in the PEC processes so as to achieve high photocurrent density and improve their efficiency. High-performance cocatalyst materials have high light transmittance, high surface active area, abundant catalytic active sites, and good conductivity.<sup>13–15</sup> To achieve these key features, ultrathin two-dimensional (2D) metal-oxide nanomaterials show great potential as ideal cocatalysts for PEC electrodes considering their atomic thickness and superior catalytic activity.<sup>16–18</sup> Indium oxide ( $\text{In}_2\text{O}_3$ ), as one of the important transition-metal oxides, can be a promising cocatalyst candidate due to its appropriate electronic structure and excellent light transmission for PEC water splitting.<sup>19–23</sup> Herein, we report the development of ultrathin mesoporous  $\text{In}_2\text{O}_3$  nanosheet cocatalysts on top of the Si NW/ $\text{TiO}_2$  photoanode. In the

Received: August 4, 2021

Accepted: October 19, 2021

Published: October 28, 2021



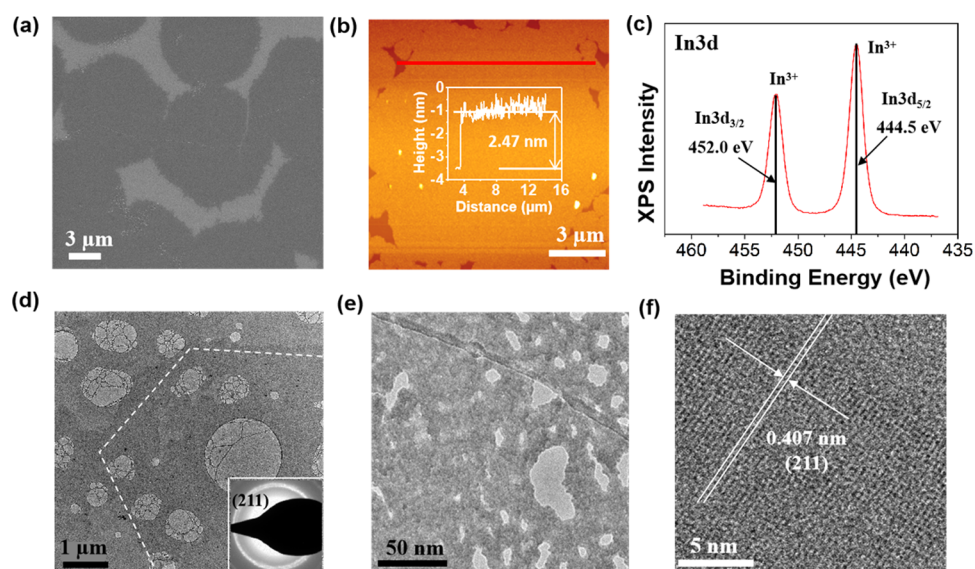


**Figure 1.** Morphology, elemental information, and structural characterization of  $\text{In}_2\text{O}_3$  nanosheets. (a) SEM image of  $\text{In}_2\text{O}_3$  nanosheets on a silicon substrate. (b) AFM topography scan of  $\text{In}_2\text{O}_3$  nanosheets. Inset is the height profile derived from the red line in (b). (c) In 3d XPS spectrum of  $\text{In}_2\text{O}_3$  nanosheets. (d) TEM image of hexagonal  $\text{In}_2\text{O}_3$  nanosheets. The inset shows the corresponding SAED pattern. (e) Enlarged TEM images showing pores on an  $\text{In}_2\text{O}_3$  nanosheet. (f) HRTEM images showing the lattice of crystalline  $\text{In}_2\text{O}_3$  domains on a nanosheet.

presence of  $\text{In}_2\text{O}_3$  nanosheets, the heterostructured photoanode exhibited an extremely low onset potential of 0.6 V vs reversible hydrogen electrode (RHE). Under 1 sun illumination, the saturated photocurrent density was significantly increased to  $36.9 \text{ mA cm}^{-2}$ , 15 times higher than that of pristine Si NWs. The substantial improvement in the PEC performance was due to the  $\text{In}_2\text{O}_3$  nanosheet coupling, which induced the largely enhanced charge injection and separation efficiency without compromising any light absorption. This work suggests that the ultrathin mesoporous  $\text{In}_2\text{O}_3$  nanosheets could be used as an efficient cocatalyst to boost the performance of regular Si nanowire-based PEC electrodes.

## EXPERIMENTAL SECTION

**Synthesis of 2.47 nm  $\text{In}_2\text{O}_3$  Nanosheets.** The ILE method was employed to synthesize 2.47 nm  $\text{In}_2\text{O}_3$  nanosheets at the water–air interface. The precursor solution was first prepared by mixing  $\text{In}(\text{NO}_3)_3$  and hexamethylenetetramine (HMTA) in 15 mL of deionized  $\text{H}_2\text{O}$ , and the concentration of both  $\text{In}(\text{NO}_3)_3$  and HMTA was 0.67 mM. The precursor solution (25 mL) was then transferred into a glass vial and allowed to stand in air for 40 min. Subsequently, the surfactant solution was prepared by mixing the chloroform solution of stearic acid (SA) and the chloroform solution of oleylamine (OAM), where the volume fractions of the SA solution and the OAM solution were 90 and 10%, respectively. The concentration of the SA solution was  $1.8 \text{ mol L}^{-1}$ , while that of the OAM solution was also  $1.8 \text{ mol L}^{-1}$  too but mixed with  $0.01 \text{ mol L}^{-1}$  hydrochloric acid. Six microliters of the as-prepared surfactant solution was then dispersed on the precursor solution surface. Ten minutes were allowed to evaporate all chloroform. The screw-cap was afterward used to seal the glass vial, and the glass vial was finally transferred into an air-dry oven at  $80 \text{ }^\circ\text{C}$ . The reaction time for the growth of 2.47 nm  $\text{In}_2\text{O}_3$  nanosheets was 100 min. A substrate was used to transfer the  $\text{In}_2\text{O}_3$  nanosheets by scooping at the solution surface and then drying at room temperature for the subsequent material characterization and PEC performance measurements.  $\text{SiO}_2$  (50 nm thick)-coated Si substrates were used for morphology characterization. The elemental chemical state characterization employed 50 nm Au-coated Si substrates. The structural characterization was based on holey carbon TEM grid substrates. For PEC performance measurements, Si NW/ $\text{TiO}_2$ , planar Si, and FTO

substrates were used to prepare test samples. The same ILE process mentioned above was performed to synthesize 5.73 nm  $\text{In}_2\text{O}_3$  nanosheets by increasing the reaction temperature to  $90 \text{ }^\circ\text{C}$  for 100 min.

### Fabrication of Si NW Arrays via the Wet Etching Method.

The metal-assisted electroless etching method was used to fabricate orientated Si NW arrays. First, an n-type Si(100) wafer was ultrasonically cleaned for 20 min by isopropanol and distilled (DI) water successively. Subsequently, the surface native oxide of the Si wafer was removed by immersing in 5 wt % HF for 30 s. Forty milliliters of a mixed solution containing 5 M HF and 0.02 M  $\text{AgNO}_3$  was prepared as the etching solution. The Si substrate was then immersed in the etching solution at room temperature for a certain time. Typically, 1 h of etching yielded  $17.8 \text{ } \mu\text{m}$  long NWs. After etching, DI water was used for cleaning the Si wafer, and then 30 min was allowed for 35 wt %  $\text{HNO}_3$  solution to remove the Ag residue on the Si wafer. At last, DI water cleaned the Si substrate again and  $\text{N}_2$  gas was employed to dry the Si substrate.

**Assembly of the Si NW/ $\text{TiO}_2$ / $\text{In}_2\text{O}_3$  Photoanodes.** Prior to  $\text{TiO}_2$  depositions, the Si NW array substrates were dipped in HF at a concentration of 5 wt % for 5 min to remove oxidized Si and contaminations.  $\text{TiO}_2$  ALD overcoating was performed in a deposition chamber. The growth conditions for one deposition cycle were 0.5 s of  $\text{H}_2\text{O}$  pulse + 60 s of  $\text{N}_2$  purging + 0.5 s of  $\text{TiCl}_4$  pulse + 60 s of  $\text{N}_2$  purging at  $120 \text{ }^\circ\text{C}$ . A  $\text{TiO}_2$  ALD coating was deposited for 50 cycles, and its growth rate was 0.1 nm/cycle. A  $\text{TiO}_2$  thin film with a thickness of about 5 nm was thus coated on the Si NW array substrates. Subsequently, the chamber was cooled to room temperature naturally under a  $\text{N}_2$  flow to obtain Si NW/ $\text{TiO}_2$  substrates. The  $\text{In}_2\text{O}_3$  nanosheets synthesized at the water–air interface were transferred onto the top of Si NW/ $\text{TiO}_2$  by directly scooping using the Si/ $\text{TiO}_2$  substrate and then dried naturally in the air to form Si NW/ $\text{TiO}_2$ / $\text{In}_2\text{O}_3$  photoanodes.

**Measurements of PEC Properties.** A three-electrode measurement configuration was used to conduct PEC measurements. The prepared electrode was employed as the working electrode, a saturated calomel electrode (SCE) as the reference electrode, and Pt wire as the counter electrode. The electrolyte of 1 M NaOH solution was used for PEC water oxidation, and the phosphate buffer solution (pH = 7) with 1 M  $\text{Na}_2\text{SO}_3$  was used for sulfite oxidation in this work.  $J_{\text{ph}}-V$  and  $J_{\text{ph}}-t$  curves were recorded using an Autolab PGSTAT302N station and measured under the illumination of an

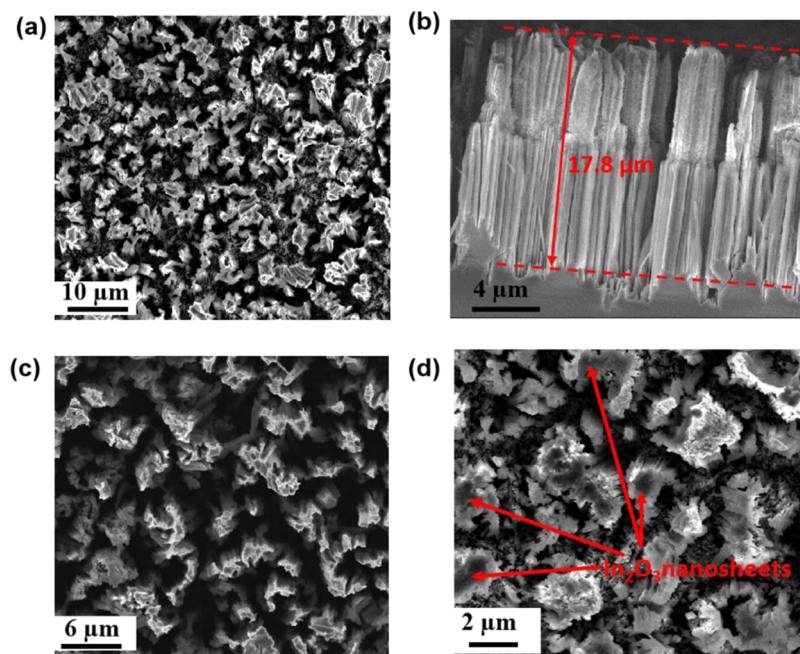


**Figure 2.** Morphology characterization of a Si/TiO<sub>2</sub>/In<sub>2</sub>O<sub>3</sub> cocatalyst. (a) Top-view SEM image of Si NW bundles. (b) Cross-sectional SEM image of Si NW bundles. (c) SEM images of Si NW bundles coated with a thin layer of ALD TiO<sub>2</sub>. (d) SEM images of Si NW bundles with In<sub>2</sub>O<sub>3</sub> nanosheets covered on top.

AM 1.5 global filter at 100 mW cm<sup>-2</sup> (one sun) with a 150 W xenon lamp. The SCE potential values were converted into values against RHE by the equation  $E(\text{RHE}) = E(\text{SCE}) + 0.244 \text{ V} + 0.059 \times \text{pH}$ . The electrochemical impedances were investigated through Solartron Electrochemical Interface SI 1287 in a 1 M NaOH solution.

**Material Characterization.** The morphologies of In<sub>2</sub>O<sub>3</sub> nanosheets and Si photoanodes were investigated through Zeiss LEO 1530 field-emission scanning electron microscope. An XE-70 Park System was used to obtain the topography images of atomic force microscopy (AFM). A Thermo Scientific K-alpha XPS instrument was used to carry out X-ray photoelectron spectroscopy (XPS) spectrum analysis. Transmission electron microscopy (TEM) measurements were performed on an FEI TF30 transmission electron microscope. A Jasco V-570 UV–vis spectrophotometer with an integrating sphere was employed to collect the reflectance spectra.

## RESULTS AND DISCUSSION

Three main steps were conducted to assemble the Si NW/TiO<sub>2</sub>/In<sub>2</sub>O<sub>3</sub> photoanode (the assembly details are included in the [Experimental Section](#)) including the preparation of the Si NW array by wet etching, TiO<sub>2</sub> ALD coating on the Si NW array, and transfer of In<sub>2</sub>O<sub>3</sub> nanosheets to the surface of Si NW/TiO<sub>2</sub>. The ionic layer epitaxy (ILE) method was employed to synthesize the mesoporous ultrathin In<sub>2</sub>O<sub>3</sub> nanosheets at the water–air interface under a monolayer of mixed stearic acid (SA) and oleyamine (OAM) surfactants at a ratio of 1:9 at 80 °C (see [Experimental Section](#) for the synthesis details). [Figure S1](#) reveals that the morphology of In<sub>2</sub>O<sub>3</sub> nanosheets was greatly affected by the surfactant mixing ratio, and the hexagonal nanosheets with the most uniform thickness were formed at an optimal ratio of 1:9. The morphology of the as-synthesized In<sub>2</sub>O<sub>3</sub> nanosheets was investigated via scanning electron microscopy (SEM). [Figure 1a](#) shows the corresponding SEM image of nanosheets on a SiO<sub>2</sub>-coated Si substrate. The densely packed In<sub>2</sub>O<sub>3</sub> nanosheets were observed and no overlaps or wrinkles were found among them, covering almost the entire surface of the Si

substrate. These nanosheets appeared to be hexagonal with diagonal lengths of  $10.5 \pm 1.1 \mu\text{m}$ . Atomic force microscopy (AFM) was used to characterize the thickness and surface flatness. [Figure 1b](#) reveals the AFM image and height profile of nanosheets, illustrating that the average thickness of the nanosheets was 2.47 nm and the surface of the nanosheets was fairly flat. As the ILE reaction temperature increased from 80 to 90 °C, the thickness increased to 5.73 nm ([Figure S2](#)). The elemental composition and chemical state in the In<sub>2</sub>O<sub>3</sub> nanosheets were confirmed by X-ray photoelectron spectroscopy (XPS), as shown in [Figure 1c](#). Two peaks at 452.0 and 444.5 eV are referred to In 3d, which coordinate to typical characteristic peaks of the In–O bonds in the cubic In<sub>2</sub>O<sub>3</sub> phase.<sup>24</sup> Thicker nanosheets exhibited similar two peaks in the XPS spectrum ([Figure S2](#)), confirming that both nanosheets were In<sub>2</sub>O<sub>3</sub>.

The crystal structure of the In<sub>2</sub>O<sub>3</sub> nanosheets was then characterized by transmission electron microscopy (TEM). Part of a hexagonal nanosheet on a TEM grid is shown in [Figure 1d](#). As marked by the dotted lines, the angle of each corner was about 120°. The edges were mostly wavy, indicating that the nanosheet was amorphous or polycrystalline. As revealed in the inset of [Figure 1d](#), the selected area electron diffraction (SAED) pattern showed relatively wide diffraction rings, consistent with the (211) plane of a typical body-centered cubic In<sub>2</sub>O<sub>3</sub>, indicating that the nanosheets were polycrystalline.<sup>25,26</sup> A zoomed-in TEM image ([Figure 1e](#)) indicated that the nanosheet had many holes with sizes from 5 to 20 nm in diameter. This mesoporous 2D morphology was possibly formed when the reduction of surface energy drove the small nuclei or initial nanosheets to merge with each other.<sup>16,27,28</sup> As shown in [Figure 1f](#), high-resolution transmission electron microscopy (HRTEM) presented the crystalline domains clearly, where the interplanar spacing was measured to be 0.407 nm, and this value corresponded to the (211) planes of cubic In<sub>2</sub>O<sub>3</sub>. A similar mesoporous polycrystal-

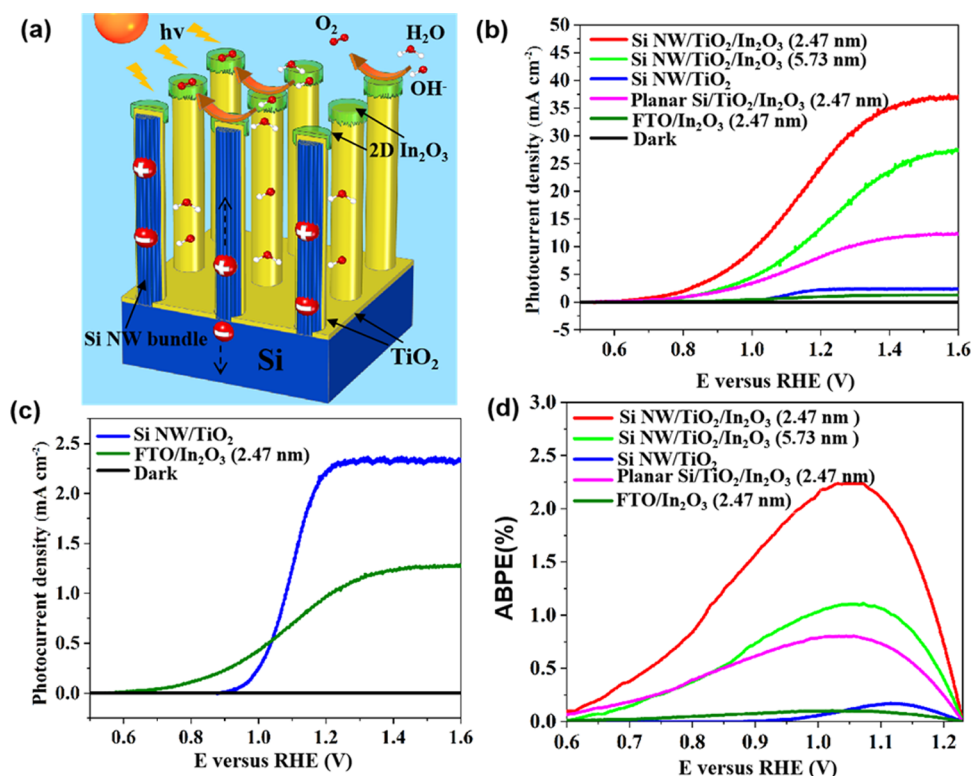


**Figure 3.** Electrochemical performance characterization and comparison. (a) Schematic of oxygen evolution processes in Si NW/TiO<sub>2</sub>/In<sub>2</sub>O<sub>3</sub> (2.47 nm). (b)  $J_{\text{ph}}-V$  curves and dark current of Si NW/TiO<sub>2</sub>/In<sub>2</sub>O<sub>3</sub> (2.47 nm), Si NW/TiO<sub>2</sub>/In<sub>2</sub>O<sub>3</sub> (5.73 nm), Si NW/TiO<sub>2</sub>, planar Si/TiO<sub>2</sub>/In<sub>2</sub>O<sub>3</sub> (2.47 nm), and FTO/TiO<sub>2</sub> photoanodes measured in 1 M NaOH electrolyte under one sun illumination. (c) Enlarged dark current and  $J_{\text{ph}}-V$  curves of Si NW/TiO<sub>2</sub> and FTO/TiO<sub>2</sub> photoanodes in (b). (d) ABPE- $V$  curves of Si NW/TiO<sub>2</sub>/In<sub>2</sub>O<sub>3</sub> (2.47 nm), Si NW/TiO<sub>2</sub>/In<sub>2</sub>O<sub>3</sub> (5.73 nm), and Si NW/TiO<sub>2</sub> photoanodes.

line structure was also observed from the thicker In<sub>2</sub>O<sub>3</sub> nanosheets (Figure S3).

Si NW arrays were fabricated via chemical etching of a Si wafer. As shown in the top-view SEM image of Si NW arrays (Figure 2a), the densely bundled Si NW was clearly observed. The average length of the as-fabricated Si NW was 17.8  $\mu\text{m}$  (Figure 2b). The entire Si NW surfaces were then completely covered by ALD (50 cycles)-coated TiO<sub>2</sub> thin film (Figure 2c). The mesoporous In<sub>2</sub>O<sub>3</sub> nanosheets synthesized at the water–air interface were directly transferred onto the top of Si NW/TiO<sub>2</sub> by directly scooping using the Si substrate. As shown in Figure 2d, the In<sub>2</sub>O<sub>3</sub> nanosheets were mostly covered on the top of Si NW bundles, forming a flat surface. Owing to their micrometer sizes, part of the nanosheets also covered the top portion of the Si NW bundles. The top portion of the Si NW bundles were the most active places on the electrode surface for PEC reactions.

The oxygen evolution process on the Si/TiO<sub>2</sub>/In<sub>2</sub>O<sub>3</sub> heterostructured photoanode surfaces is schematically demonstrated in Figure 3a. The electrons and holes were produced in the Si NW arrays when Si NW absorbed photons under light illumination. The holes were driven to migrate through the TiO<sub>2</sub> film by an in-built electric field in the depletion region at the interface of the cocatalyst/electrolyte, oxidizing the hydroxyl groups in the electrolyte; while the protons were reduced by transferred electrons at the counter electrode.<sup>7,14</sup> These charge separation and transfer processes were further displayed in the energy band diagram (Figure S4). To investigate the PEC performance of Si NW/TiO<sub>2</sub>/In<sub>2</sub>O<sub>3</sub> photoanode, the photocurrent density–potential ( $J_{\text{ph}}-V$ )

curves were measured in the electrolyte of 1 M sodium hydroxide (NaOH) under one sun illumination. As a comparison, the  $J_{\text{ph}}-V$  curves of Si/TiO<sub>2</sub> without In<sub>2</sub>O<sub>3</sub> nanosheets coating, planar Si/TiO<sub>2</sub>/In<sub>2</sub>O<sub>3</sub> (2.47 nm), and FTO/TiO<sub>2</sub> photoanodes were also characterized under the same conditions. As shown in Figure 3b, the cocatalyst with 2.47 nm In<sub>2</sub>O<sub>3</sub> nanosheets showed a low onset potential of 0.6 V vs reversible hydrogen electrode (RHE), which reached the lowest value reported on Si-based photoanodes for the PEC oxygen evolution reactions (OERs) (Table S1). This low onset potential was also much lower than those of the typical Ni-based cocatalyst-coated similar Si/TiO<sub>2</sub> photoanodes such as Si/TiO<sub>2</sub>/Ni (0.85 V vs RHE),<sup>15</sup> Si/TiO<sub>x</sub>/ITO/NiOOH (0.9 V vs RHE),<sup>29</sup> Si/TiO<sub>x</sub>/NiCrO<sub>x</sub> (1.07 V vs RHE),<sup>11</sup> and Si/TiO<sub>x</sub>/Ni (1.2 V vs RHE).<sup>12</sup> Moreover, the onset potential increased to 0.65 V vs RHE with the increase in the nanosheet thickness to 5.73 nm, suggesting the possible higher resistance from the thicker In<sub>2</sub>O<sub>3</sub> coverage. Nevertheless, onset potentials of both nanosheet-coated samples were significantly lower than those of Si NW/TiO<sub>2</sub> photoanodes without the nanosheet coating (0.9 V vs RHE; Figure 3c), confirming that loading of In<sub>2</sub>O<sub>3</sub> nanosheets as a cocatalyst could greatly facilitate interfacial photoelectrochemical reactions. When the Si NW array substrate was switched to planar Si, the planar Si/TiO<sub>2</sub>/In<sub>2</sub>O<sub>3</sub> (2.47 nm) still showed a relatively low onset potential of 0.68 V vs RHE, although this value was larger than that of Si NW/TiO<sub>2</sub>/In<sub>2</sub>O<sub>3</sub> (2.47 nm). Furthermore, the loading of In<sub>2</sub>O<sub>3</sub> nanosheets even caused the FTO/TiO<sub>2</sub> photoanodes to exhibit a lower onset potential of 0.57 V vs RHE than that of Si NW/TiO<sub>2</sub>/In<sub>2</sub>O<sub>3</sub> (2.47 nm), further evidencing the advantages

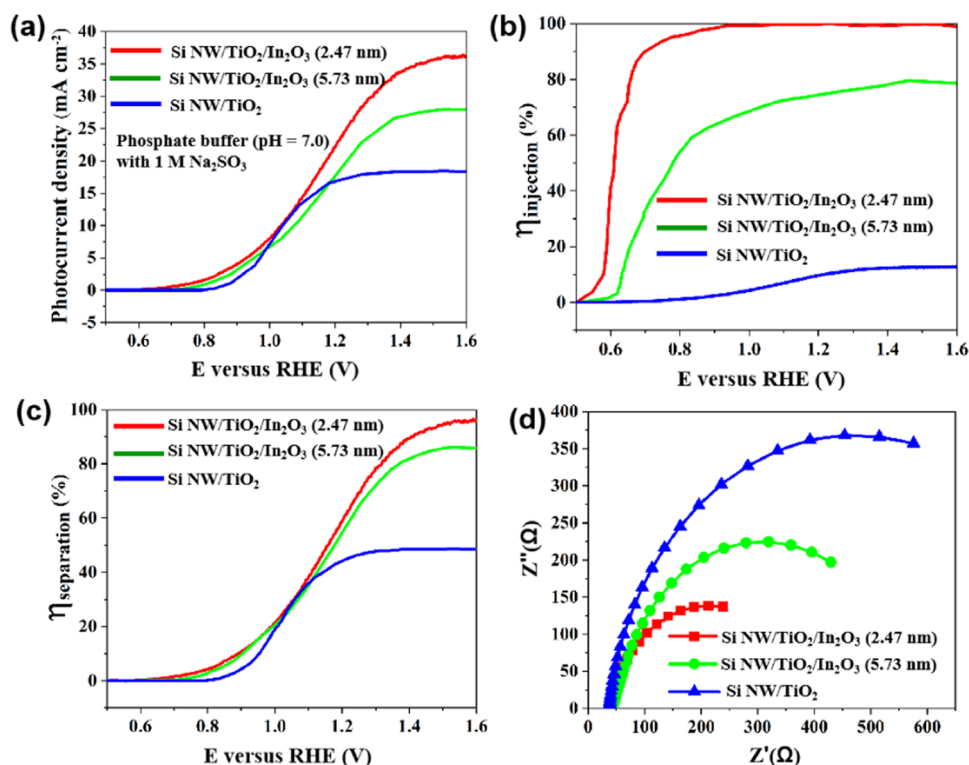


**Figure 4.** Injection efficiency and charge separation efficiency. (a)  $J_{\text{ph}}-V$  curves of Si NW/TiO<sub>2</sub>/In<sub>2</sub>O<sub>3</sub> (2.47 nm), Si NW/TiO<sub>2</sub>/In<sub>2</sub>O<sub>3</sub> (5.73 nm), and Si NW/TiO<sub>2</sub> for sulfite oxidation measured in phosphate buffer (pH = 7) with 1 M Na<sub>2</sub>SO<sub>3</sub> as the hole scavenger under one sun illumination. Their respective (b) injection efficiency, (c) charge separation efficiency, and (d) electrochemical impedance spectroscopy (EIS) plots were measured at 1.23 V vs RHE.

of ultrathin In<sub>2</sub>O<sub>3</sub> nanosheet cocatalysts in reducing the onset potential.

Accordingly,  $J_{\text{ph}}$  also exhibited a remarkable enhancement with In<sub>2</sub>O<sub>3</sub> nanosheet coating. As shown in Figure 3b, the Si NW/TiO<sub>2</sub>/In<sub>2</sub>O<sub>3</sub> (2.47 nm) photoanodes showed a  $J_{\text{ph}}$  of 27 mA cm<sup>-2</sup> at 1.23 V vs RHE, and a saturation  $J_{\text{ph}}$  of 36.9 mA cm<sup>-2</sup>. This  $J_{\text{ph}}$  value at 1.23 vs RHE was more than 1 order of magnitude higher than those from Si NW/TiO<sub>2</sub> photoanodes (2.3 mA cm<sup>-2</sup>) and FTO/TiO<sub>2</sub> photoanodes (1.1 mA cm<sup>-2</sup>) at the same potential. It was also among the largest reported  $J_{\text{ph}}$  values for Si-based photoanodes (Table S1) and even much larger than that of typical Ni-based cocatalyst-coated similar Si photoanodes such as n-Si/TiO<sub>x</sub>/ITO/NiOOH (16 mA cm<sup>-2</sup>),<sup>29</sup> np<sup>+</sup>-Si/TiO<sub>x</sub>/NiCrO<sub>x</sub> (3.6 mA cm<sup>-2</sup>),<sup>11</sup> and n-Si/TiO<sub>x</sub>/Ni (1 mA cm<sup>-2</sup>).<sup>12</sup> As the thickness of the In<sub>2</sub>O<sub>3</sub> nanosheets increased to 5.73 nm,  $J_{\text{ph}}$  was substantially reduced to 15.2 mA cm<sup>-2</sup> at 1.23 V vs RHE and the saturated  $J_{\text{ph}}$  was reduced to 27.4 mA cm<sup>-2</sup>. Meanwhile, when Si NW substrate became planar Si, the prepared planar Si/TiO<sub>2</sub>/In<sub>2</sub>O<sub>3</sub> (2.47 nm) exhibited a greatly reduced  $J_{\text{ph}}$  of 8.9 mA cm<sup>-2</sup> at 1.23 V vs RHE, but this  $J_{\text{ph}}$  value was much larger than that of Si/TiO<sub>2</sub> without the In<sub>2</sub>O<sub>3</sub> nanosheet coating. The applied bias photon-to-current efficiency (ABPE) was then estimated by the equation  $\text{ABPE} = J_{\text{ph}}(1.23 \text{ V vs RHE} - E)/P_{\text{in}}$ , where  $P_{\text{in}}$  is the incident light intensity (100 mW cm<sup>-2</sup>).<sup>8,29</sup> The ABPE- $V$  curves are compared in Figure 3d. The ABPE of all of the samples showed a trend of first increasing and then decreasing as the potential increased from 0.6 V vs RHE to 1.23 V vs RHE. The Si NW/TiO<sub>2</sub>/In<sub>2</sub>O<sub>3</sub> (2.47 nm) photoanodes exhibited a maximum ABPE of 2.25% at 1.03 V vs RHE. This efficiency is more than twice that of thicker In<sub>2</sub>O<sub>3</sub>-coated Si NWs (1.11%), 13 times that of Si NWs without an In<sub>2</sub>O<sub>3</sub>

nanosheet coating (0.17%), and 20 times that of FTO/In<sub>2</sub>O<sub>3</sub> (0.11%). Although the maximum ABPE (0.81%) of planar Si/TiO<sub>2</sub>/In<sub>2</sub>O<sub>3</sub> (2.47 nm) was lower than that of Si NW/TiO<sub>2</sub>/In<sub>2</sub>O<sub>3</sub> (2.47 nm), it was nearly 5 times that of Si/TiO<sub>2</sub> without an In<sub>2</sub>O<sub>3</sub> nanosheet coating. The maximum efficiency achieved by our Si/TiO<sub>2</sub>/In<sub>2</sub>O<sub>3</sub> cocatalyst surpassed those of most of the reported Si-based photoanodes (Table S1), evidencing the substantial performance gain by the In<sub>2</sub>O<sub>3</sub> nanosheet cocatalyst.

To understand the enhancement effect introduced by the ultrathin mesoporous In<sub>2</sub>O<sub>3</sub> nanosheets, a few key PEC parameters including  $\eta_{\text{absorption}}$ ,  $\eta_{\text{injection}}$ , and  $\eta_{\text{separation}}$  were investigated, where  $\eta_{\text{absorption}}$  is the light absorption efficiency,  $\eta_{\text{injection}}$  is the hole injection efficiency, and  $\eta_{\text{separation}}$  is the electron-hole separation efficiency. Specifically,  $J_{\text{ph}} = J_{\text{abs}} \times \eta_{\text{injection}} \times \eta_{\text{separation}}$ , where  $J_{\text{abs}}$  is the photocurrent density at 100% internal quantum efficiency. ABPE can also be expressed as the product of  $\eta_{\text{absorption}}$ ,  $\eta_{\text{injection}}$ , and  $\eta_{\text{separation}}$ .<sup>13</sup>

As shown in Figure S5a, the light reflection spectra of all photoanodes were measured to extract their  $\eta_{\text{absorption}}$ . Figure S5b shows their corresponding ultraviolet-visible  $\eta_{\text{absorption}}$  derived from the reflection spectra. Little difference in  $\eta_{\text{absorption}}$  was observed for Si/TiO<sub>2</sub>/In<sub>2</sub>O<sub>3</sub> (2.47 nm) and Si/TiO<sub>2</sub> samples, where both exhibited an average  $\eta_{\text{absorption}}$  of ~94.5% in the ultraviolet, visible, and near-infrared regions. However, Si/TiO<sub>2</sub> NWs coated with thicker (5.73 nm) In<sub>2</sub>O<sub>3</sub> nanosheets exhibited an obviously lower average  $\eta_{\text{absorption}}$  of ~84%. These measurements suggested that the loading of ultrathin In<sub>2</sub>O<sub>3</sub> nanosheets did not impact the light absorption of Si NW structures, while a slight increase in the nanosheet thickness to ~5 nm would substantially reduce the light absorption of the photoanode. In addition, the difference in

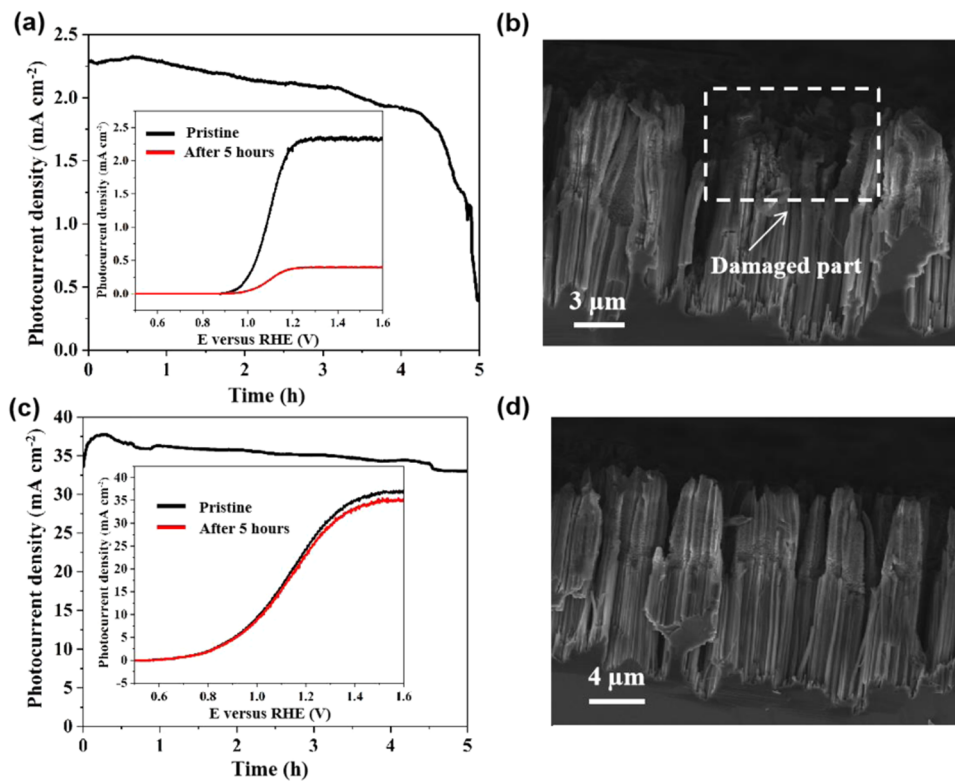


**Figure 5.** Stability evaluation. (a) Photocurrent density–time ( $J_{\text{ph}}-t$ ) curves of Si NW/TiO<sub>2</sub> at a constant 1.6 V vs RHE. Insets are  $J_{\text{ph}}-V$  curves before and after 5 h of PEC water oxidation. (b) Cross-sectional SEM images of Si NW/TiO<sub>2</sub> photoanodes after 5 h of PEC water oxidation. (c)  $J_{\text{ph}}-t$  curves of Si NW/TiO<sub>2</sub>/In<sub>2</sub>O<sub>3</sub> (2.47 nm) at a constant voltage of 1.6 V vs RHE. Insets are  $J_{\text{ph}}-V$  curves before and after 5 h of PEC water oxidation. (d) Cross-sectional SEM images of Si NW/TiO<sub>2</sub>/2.47 nm In<sub>2</sub>O<sub>3</sub> photoanodes after 5 h of PEC water oxidation.

$\eta_{\text{absorption}}$  between the two In<sub>2</sub>O<sub>3</sub>-coated samples matched well with their  $J_{\text{ph}}$  and ABPE variation (Figure 3b,d), implying that photon absorption could be the main factor responsible for nanosheet-thickness-related  $J_{\text{ph}}$  and ABPE variations.  $J_{\text{abs}}$  was calculated by integrating the electron flux of the photoanodes across the 300–1200 nm wavelength range (Figure S5c,d).<sup>7,30</sup> Si NWs exhibited nearly the same  $J_{\text{abs}}$  when they were covered by thin In<sub>2</sub>O<sub>3</sub> nanosheets (37.8 vs 37.9 mA cm<sup>-2</sup>), while thick In<sub>2</sub>O<sub>3</sub> nanosheets reduced  $J_{\text{abs}}$  to 32.5 mA cm<sup>-2</sup>. This result further confirmed that the  $J_{\text{ph}}$  reduction from 5.73 nm In<sub>2</sub>O<sub>3</sub> nanosheets coverage was primarily due to reduced light absorption.

The  $J_{\text{ph}}-V$  curves (Figure 4a) were also measured in phosphate buffer (pH = 7) with 1 M Na<sub>2</sub>SO<sub>3</sub> to investigate the corresponding injection efficiency ( $\eta_{\text{injection}}$ ) and separation efficiency ( $\eta_{\text{separation}}$ ). Since sulfite was a hole scavenger, it can be assumed that the photogenerated holes are completely consumed when they arrived at the interface of electrode/electrolyte, i.e.,  $\eta_{\text{injection}} = 100\%$ . Therefore, the photocurrent density measured with sulfite in the electrolyte is given by  $J_{\text{sulfite}} = J_{\text{abs}}\eta_{\text{separation}}$ . Therefore, the injection and separation efficiencies can be defined as  $\eta_{\text{injection}} = J_{\text{ph}}/J_{\text{sulfite}}$  and  $\eta_{\text{separation}} = J_{\text{sulfite}}/J_{\text{abs}}$ , respectively.<sup>7,29,31,32</sup>

$\eta_{\text{injection}}$  as a function of applied bias was thus calculated and presented in Figure 4b. The highest  $\eta_{\text{injection}}$  of ~100% was obtained from Si/TiO<sub>2</sub>/In<sub>2</sub>O<sub>3</sub> (2.47 nm) at >0.95 V vs RHE, suggesting all of the holes accumulated at the top of Si NW/TiO<sub>2</sub> can be consumed for the PEC OER under this bias. Without In<sub>2</sub>O<sub>3</sub> coating,  $\eta_{\text{injection}}$  was only 10.4% at 1.23 V vs RHE, indicating the overall  $J_{\text{ph}}$  and ABPE were enhanced primarily because of the substantially improved hole injection

efficiency. Such a big improvement of  $\eta_{\text{injection}}$  might be due to the high OER catalytic activity of ultrathin mesoporous In<sub>2</sub>O<sub>3</sub> nanosheets, where the ultrasmall thickness resulted in extremely short charge diffusion length and thus accelerated holes transfer from Si NW arrays to nanosheet surfaces.<sup>16,33,34</sup> The mesoporous morphology might further boost the OER activity by increasing the surface catalytic active areas.<sup>35–38</sup> In addition, 5.73 nm In<sub>2</sub>O<sub>3</sub> only yielded 75.2%  $\eta_{\text{injection}}$  at 1.23 V vs RHE, suggesting that the hole injection efficiency was very sensitive to the nanosheet thickness likely due to the nanoscale crystalline phase.

Based on the  $J_{\text{ph}}-V$  curves for sulfite oxidation, the  $\eta_{\text{separation}}$  values were also calculated as shown in Figure 4c. The sample coated with 2.47 nm In<sub>2</sub>O<sub>3</sub> nanosheet exhibited a high  $\eta_{\text{separation}}$  of 65.5% at 1.23 V vs RHE, which maximized at 96.2% when the bias reached 1.6 V vs RHE. Without In<sub>2</sub>O<sub>3</sub> nanosheets, the Si/TiO<sub>2</sub> photoanode only had 45%  $\eta_{\text{separation}}$  at 1.23 V vs RHE. Meanwhile, thicker In<sub>2</sub>O<sub>3</sub> nanosheets also lowered  $\eta_{\text{separation}}$  to 85.9%. This comparison suggested that the In<sub>2</sub>O<sub>3</sub> nanosheet cocatalyst could largely promote the electrons and holes to separate and produce more surface-reaching holes. A much smaller semicircle radius of the sample coated with 2.47 nm In<sub>2</sub>O<sub>3</sub> in electrochemical impedance spectroscopy was obtained (Figure 4d), confirming that the hole transfer across the heterostructured material interfaces was substantially promoted by the In<sub>2</sub>O<sub>3</sub> nanosheet cocatalysts; 5.73 nm In<sub>2</sub>O<sub>3</sub> exhibited a higher impedance likely due to the slightly longer diffusion length through the thickness direction. This observation further confirmed the critical requirement of the nanometer-scale thickness of the cocatalysts. In addition, the high  $\eta_{\text{injection}}$  induced by In<sub>2</sub>O<sub>3</sub> nanosheets led to the rapid

consumption of the surface-reaching holes, which was also favorable to achieving a high electron/hole separation rate.

In addition to promoting the photoelectrochemical performance, loading of ultrathin  $\text{In}_2\text{O}_3$  nanosheet cocatalysts also improved the stability of Si/TiO<sub>2</sub> photoanodes in an electrolyte. Figure 5 compares the stability of the Si/TiO<sub>2</sub> photoanodes with and without  $\text{In}_2\text{O}_3$  nanosheets by measuring their corresponding photocurrent density–time ( $J_{\text{ph}}-t$ ) curves in 1 M NaOH at a constant external bias of 1.6 V vs RHE. Without the  $\text{In}_2\text{O}_3$  nanosheet cocatalysts, the Si/TiO<sub>2</sub> photoanodes exhibited a 10% decrease of  $J_{\text{ph}}$  within 2.5 h (Figure 5a). The even sharper deterioration occurred after 4.5 h, leading to an 83% loss of  $J_{\text{ph}}$  after 5 h of operation. The  $J_{\text{ph}}-V$  curves showed a significant decay after 5 h of PEC water oxidation (Figure 5a inset). This rapid decay of  $J_{\text{ph}}$  could be attributed to the corrosion damage in part of Si NW bundles (Figure 5b). After loading of  $\text{In}_2\text{O}_3$  nanosheet cocatalysts, the Si/TiO<sub>2</sub>/ $\text{In}_2\text{O}_3$  photoanode maintained 90%  $J_{\text{ph}}$  after 5 h of continuous operation (Figure 5c). In addition, only a slight decay was shown in the  $J_{\text{ph}}-V$  curves after the PEC test (Figure 5c inset), further confirming the appropriate function of  $\text{In}_2\text{O}_3$  nanosheet cocatalysts during the long-term operation. The cross-sectional SEM images in Figure 5d reveal that Si NW bundles retained nearly the same morphology after the test, and the top-view SEM images (Figure S6) further confirmed that  $\text{In}_2\text{O}_3$  nanosheets were still covered the top of Si NW bundles. Although the  $\text{In}_2\text{O}_3$  nanosheets did not cover the entire NW surfaces, the rapid charge transfer and consumption at the preferred  $\text{In}_2\text{O}_3$  nanosheet surface may limit the photoelectrochemical corrosion in surface channels.

## CONCLUSIONS

In summary, we developed a high-performance heterostructured Si NW- $\text{In}_2\text{O}_3$  nanosheet cocatalyst for PEC water splitting. The mesoporous ultrathin  $\text{In}_2\text{O}_3$  nanosheets covered the top of Si NW bundles. Combined with an intermediate protective layer of ALD TiO<sub>2</sub> thin film, the Si/TiO<sub>2</sub>/ $\text{In}_2\text{O}_3$  photoanode exhibited a low onset potential of 0.6 V vs RHE, which was among the lowest value reported for Si-based photoanodes for the PEC OER. A high saturated photocurrent density of 36.9 mA cm<sup>-2</sup>, photocurrent density of 27 mA cm<sup>-2</sup> at 1.23 V vs RHE, and applied bias photon-to-current efficiency of 2.25% were obtained from Si NW photoanodes covered with the 2.47 nm  $\text{In}_2\text{O}_3$  nanosheet. They were more than 1 order of magnitude higher than those of the Si NW/TiO<sub>2</sub> photoanode without the  $\text{In}_2\text{O}_3$  nanosheet coating. By comparing their light absorption, hole injection, and charge separation properties, the substantial improvements in the PEC performance from the  $\text{In}_2\text{O}_3$  nanosheet cocatalysts were found to be the result of the enhanced charge injection and charge separation efficiencies. It was also found critical to have the nanosheet thickness less than a few nanometers to achieve high optical transparency as well as to minimize the charge transport impedance. In addition, applying  $\text{In}_2\text{O}_3$  nanosheet cocatalysts also can protect the Si NW/TiO<sub>2</sub> electrode from corrosive photoelectrochemical reactions, contributing to an improvement of operational stability. This research provides an effective pathway to the design of high-performance Si-based PEC photoanodes by integrating ultrathin nanosheet cocatalysts, bringing in a new promise for highly efficient solar-fuel conversion.

## ASSOCIATED CONTENT

### Supporting Information

The Supporting Information is available free of charge at <https://pubs.acs.org/doi/10.1021/acsami.1c14865>.

Influence of surfactant ratio on the morphology of  $\text{In}_2\text{O}_3$  nanosheets; morphology and elemental information of 5.73 nm  $\text{In}_2\text{O}_3$  nanosheets; structural characterization of 5.73 nm  $\text{In}_2\text{O}_3$  nanosheets; schematic energy band diagram; absorption spectra and electron flux; top-view SEM images of Si NW/TiO<sub>2</sub>/2.47 nm  $\text{In}_2\text{O}_3$  photoanodes after 5 h of PEC water oxidations; and PEC performance comparison between this work and the recently reported silicon photoanodes (PDF)

## AUTHOR INFORMATION

### Corresponding Authors

**Guangyuan Yan** – School of Mechanical, Electronic and Control Engineering, Beijing Jiaotong University, Beijing 100044, China; [orcid.org/0000-0002-1080-0138](https://orcid.org/0000-0002-1080-0138); Email: [ygyuan@bjtu.edu.cn](mailto:ygyuan@bjtu.edu.cn)

**Shuming Xing** – School of Mechanical, Electronic and Control Engineering, Beijing Jiaotong University, Beijing 100044, China; Email: [smxing@bjtu.edu.cn](mailto:smxing@bjtu.edu.cn)

**Xudong Wang** – Department of Material Sciences and Engineering, University of Wisconsin-Madison, Madison, Wisconsin 53706, United States; [orcid.org/0000-0002-9762-6792](https://orcid.org/0000-0002-9762-6792); Email: [xudong@engr.wisc.edu](mailto:xudong@engr.wisc.edu)

### Authors

**Yutao Dong** – Department of Material Sciences and Engineering, University of Wisconsin-Madison, Madison, Wisconsin 53706, United States; [orcid.org/0000-0003-3582-087X](https://orcid.org/0000-0003-3582-087X)

**Tong Wu** – School of Mechanical, Electronic and Control Engineering, Beijing Jiaotong University, Beijing 100044, China

Complete contact information is available at: <https://pubs.acs.org/doi/10.1021/acsami.1c14865>

### Notes

The authors declare no competing financial interest.

## ACKNOWLEDGMENTS

This work was partially supported by the Natural Science Foundation of Beijing Municipality (2214075) and the Fundamental Research Funds for the Central Universities (2021JBM019). Nanosheet synthesis and photoanode assembly were supported by the U.S. Department of Energy (DOE), Office of Science, Basic Energy Sciences (BES), under Award No. DE-SC0020283.

## REFERENCES

- (1) He, B.; Jia, S. R.; Zhao, M. Y.; Wang, Y.; Chen, T.; Zhao, S. Q.; Li, Z.; Lin, Z. Q.; Zhao, Y. L.; Li, X. Q. General and Robust Photothermal-Heating-Enabled High-Efficiency Photoelectrochemical Water Splitting. *Adv. Mater.* **2021**, *33*, No. 2004406.
- (2) Meng, L. X.; Wang, M.; Sun, H. X.; Tian, W.; Xiao, C. H.; Wu, S. H.; Cao, F. R.; Li, L. Designing a Transparent CdIn<sub>2</sub>S<sub>4</sub>/In<sub>2</sub>S<sub>3</sub> Bulk-Heterojunction Photoanode Integrated with a Perovskite Solar Cell for Unbiased Water Splitting. *Adv. Mater.* **2020**, *32*, No. 2002893.
- (3) Sokol, K. P.; Ruff, A.; Zhang, J. Z.; Robinson, W. E.; Warnan, J. L.; Kornienko, N.; Nowaczyk, M. M.; Reisner, E. Bias-Free Photoelectrochemical Water Splitting with Photosystem II on a

Dye-Sensitized Photoanode Wired to Hydrogenase. *Nat. Energy* **2018**, *3*, 944–951.

(4) Lewis, N. S. Research Opportunities to Advance Solar Energy Utilization. *Science* **2016**, *351*, No. aad1920.

(5) Joya, K. S.; Joya, Y. F.; Kasim, O.; Krol, R. V. D. Water-Splitting Catalysis and Solar Fuel Devices: Artificial Leaves on the Move. *Angew. Chem., Int. Ed.* **2013**, *52*, 10426–10437.

(6) Liu, C.; Colón, B. C.; Ziesack, M.; Silver, P. A.; Nocera, D. G. Water Splitting-biosynthetic System with CO<sub>2</sub> Reduction Efficiencies Exceeding Photosynthesis. *Science* **2016**, *352*, 1210–1213.

(7) Yu, Y. H.; Zhang, Z.; Yin, X.; Kvit, A.; Liao, Q. L.; Kang, Z.; Yan, X. Q.; Zhang, Y.; Wang, X. D. Enhanced Photoelectrochemical Efficiency and Stability Using a Conformal TiO<sub>2</sub> Silicon Photoanode. *Nat. Energy* **2017**, *2*, No. 17045.

(8) Shi, J.; Hara, Y.; Sun, C. L.; Anderson, A. M.; Wang, X. D. Three-Dimensional High-Density Hierarchical Nanowire Architecture for High-Performance Photoelectrochemical Electrodes. *Nano Lett.* **2011**, *11*, 3413–3419.

(9) Ghosh, D.; Roy, K.; Sarkar, K.; Devi, P.; Kumar, P. Surface Plasmon-Enhanced Carbon Dot-Embellished Multifaceted Si(111) Nanoheterostructure for Photoelectrochemical Water Splitting. *ACS Appl. Mater. Interfaces* **2020**, *12*, 28792–28800.

(10) Roy, K.; Ghosh, D.; Sarkar, K.; Devi, P.; Kumar, P. Chlorophyll(a)/Carbon Quantum Dot Bio-Nanocomposite Activated Nano-Structured Silicon as an Efficient Photocathode for Photoelectrochemical Water Splitting. *ACS Appl. Mater. Interfaces* **2020**, *12*, 37218–37226.

(11) Verlage, E.; Hu, S.; Liu, R.; Jones, R. J. R.; Sun, K.; Xiang, C. X.; Lewis, N. S.; Atwater, H. A. A Monolithically Integrated, Intrinsically Safe, 10% Efficient, Solar-Driven Water-Splitting System Based on Active, Stable Earth-Abundant Electrocatalysts in Conjunction with Tandem III-V Light Absorbers Protected by Amorphous TiO<sub>2</sub> Films. *Energy Environ. Sci.* **2015**, *8*, 3166–3172.

(12) McDowell, M. T.; Lichterman, M. F.; Carim, A. I.; Liu, R.; Hu, S.; Brunschwig, B. S.; Lewis, N. S. The Influence of Structure and Processing on the Behavior of TiO<sub>2</sub> Protective Layers for Stabilization of n-Si/TiO<sub>2</sub>/Ni Photoanodes for Water Oxidation. *ACS Appl. Mater. Interfaces* **2015**, *7*, 15189–15199.

(13) Ding, C. M.; Shi, J. Y.; Wang, Z. L.; Li, C. Photoelectrocatalytic Water Splitting: Significance of Cocatalysts, Electrolyte, and Interfaces. *ACS Catal.* **2017**, *7*, 675–688.

(14) Thalluri, S. M.; Bai, L. C.; Lv, C. C.; Huang, Z. P.; Hu, XiL.; Liu, L. F. Strategies for Semiconductor/Electrocatalyst Coupling towards Solar-Driven Water Splitting. *Adv. Sci.* **2020**, *7*, No. 1902102.

(15) Liu, B.; Feng, S. J.; Yang, L. F.; Li, C. C.; Luo, Z. B.; Wang, T.; Gong, J. L. Bifacial Passivation of n-Silicon Metal-Insulator-Semiconductor Photoelectrodes for Efficient Oxygen and Hydrogen Evolution Reactions. *Energy Environ. Sci.* **2020**, *13*, 221–228.

(16) Yan, G. Y.; Wang, Y. Z.; Zhang, Z. Y.; Dong, Y. T.; Wang, J. Y.; Carlos, C.; Zhang, P.; Cao, Z. Q.; Mao, Y. C.; Wang, X. D. Nanoparticle-Decorated Ultrathin La<sub>2</sub>O<sub>3</sub> Nanosheets as an Efficient Electrocatalysis for Oxygen Evolution Reactions. *Nano-Micro Lett.* **2020**, *12*, No. 49.

(17) Wang, Y. Z.; Zhang, Z. Y.; Mao, Y. C.; Wang, X. D. Two-Dimensional Nonlayered Materials for Electrocatalysis. *Energy Environ. Sci.* **2020**, *13*, 3993–4016.

(18) Zhu, Y.; Peng, L. L.; Fang, Z. W.; Yan, C. S.; Zhang, X.; Yu, G. H. Structural Engineering of 2D Nanomaterials for Energy Storage and Catalysis. *Adv. Mater.* **2018**, *30*, No. 1706347.

(19) Zhu, L.; He, G.; Long, Y. T.; Yang, B.; Lv, J. G. Eco-Friendly, Water-Induced In<sub>2</sub>O<sub>3</sub> Thin Films for High-Performance Thin-Film Transistors and Inverters. *IEEE Trans. Electron Devices* **2018**, *65*, 2870–2876.

(20) Yang, H. R.; Tian, J.; Bo, Y. Y.; Zhou, Y. L.; Wang, X. Z.; Cui, H. Visible Photocatalytic and Photoelectrochemical Activities of TiO<sub>2</sub> Nanobelts Modified by In<sub>2</sub>O<sub>3</sub> Nanoparticles. *J. Colloid Interface Sci.* **2017**, *487*, 258–265.

(21) He, L.; Wood, E. T.; Wu, B.; Dong, Y. C.; Hoch, B. L.; Reyes, M. L.; Wang, D.; Kübel, C.; Qian, C. X.; Jia, J.; Liao, K.; O'Brien, G.

P.; Sandhel, A.; Loh, Y. Y. J.; Szymanski, P.; Kherani, P. N.; Sum, C. T.; Mims, A. C.; Ozin, A. G. Spatial Separation of Charge Carriers in In<sub>2</sub>O<sub>3-x</sub>(OH)<sub>y</sub> Nanocrystal Superstructures for Enhanced Gas-Phase Photocatalytic Activity. *ACS Nano* **2016**, *10*, 5578–5586.

(22) Zhang, Y.; Jiang, C. H.; Zhuang, S.; Lu, M.; Cai, Y. C. Mesoporous In<sub>2</sub>O<sub>3</sub> Nanofibers Assembled by Ultrafine Nanoparticles as a High Capacity Anode for Li-ion Batteries. *RSC Adv.* **2016**, *6*, 49782–49786.

(23) Li, L.; Jiang, G. X.; Sun, R. Z.; Cao, B. Q. Two-Dimensional Porous Co<sub>3</sub>O<sub>4</sub> Nanosheets for High-Performance Lithium Ion Batteries. *New J. Chem.* **2017**, *41*, 15283–15288.

(24) Lei, F. C.; Sun, Y. F.; Liu, K. T.; Gao, S.; Liang, L.; Pan, B. C.; Xie, Y. Oxygen Vacancies Confined in Ultrathin Indium Oxide Porous Sheets for Promoted Visible-Light Water Splitting. *J. Am. Chem. Soc.* **2014**, *136*, 6826–6829.

(25) Ren, Y.; Zhou, X. R.; Luo, W.; Xu, P. C.; Zhu, Y. R.; Li, X. X.; Cheng, X. W.; Deng, Y. H.; Zhao, D. Y. Amphiphilic Block Copolymer Templated Synthesis of Mesoporous Indium Oxides with Nanosheet-Assembled Pore Walls. *Chem. Mater.* **2016**, *28*, 7997–8005.

(26) Liu, D.; Lei, W. W.; Qin, S.; Hou, L. T.; Liu, Z. W.; Cui, Q. L.; Chen, Y. Large-Scale Synthesis of Hexagonal Corundum-Type In<sub>2</sub>O<sub>3</sub> by Ball Milling with Enhanced Lithium Storage Capabilities. *J. Mater. Chem. A* **2013**, *1*, 5274–5278.

(27) Peng, L. L.; Xiong, P.; Ma, L.; Yuan, Y. F.; Zhu, Y.; Chen, D. H.; Luo, X. Y.; Lu, J.; Amine, K.; Yu, G. H. Holey Two-Dimensional Transition Metal Oxide Nanosheets for Efficient Energy Storage. *Nat. Commun.* **2017**, *8*, No. 15139.

(28) Yan, G. Y.; Wang, Y. Z.; Zhang, Z. Y.; Li, J.; Carlos, C.; German, N. L.; Zhang, C. Y.; Wang, J. Y.; Voyles, M. P.; Wang, X. D. Enhanced Ferromagnetism from Organic-Cerium Oxide Hybrid Ultrathin Nanosheets. *ACS Appl. Mater. Interfaces* **2019**, *11*, 44601–44608.

(29) Yao, T. T.; Chen, R. T.; Li, J. J.; Han, J. F.; Qin, W.; Wang, H.; Shi, J. Y.; Fan, F. T.; Li, C. Manipulating the Interfacial Energetics of n-Type Silicon Photoanode for Efficient Water Oxidation. *J. Am. Chem. Soc.* **2016**, *138*, 13664–13672.

(30) Fu, H. C.; Varadhan, P.; Lin, C. H.; He, J. H. Spontaneous Solar Water Splitting with Decoupling of Light Absorption and Electrocatalysis Using Silicon Back-Buried Junction. *Nat. Commun.* **2020**, *11*, No. 3930.

(31) Jian, J. X.; Jokubavicius, V.; Syväjärvi, M.; Yakimova, R.; Sun, J. W. Nanoporous Cubic Silicon Carbide Photoanodes for Enhanced Solar Water Splitting. *ACS Nano* **2021**, *15*, 5502–5512.

(32) Lee, S. A.; Lee, T. H.; Kim, C. Y.; Choi, M. J.; Park, H.; Choi, S.; Lee, J.; Oh, J.; Kim, S. Y.; Jang, H. W. Amorphous Cobalt Oxide Nanowalls as Catalyst and Protection Layers on n-Type Silicon for Efficient Photoelectrochemical Water Oxidation. *ACS Catal.* **2020**, *10*, 420–429.

(33) Luo, Z. B.; Wang, T.; Gong, J. L. Single-Crystal Silicon-Based Electrodes for Unbiased Solar Water Splitting: Current Status and Prospects. *Chem. Soc. Rev.* **2019**, *48*, 2158–2181.

(34) Karuturi, S. K.; Shen, H. P.; Sharma, A.; Beck, J. F.; Varadhan, P.; The, D.; Narangari, R. P.; Zhang, D. D.; Wan, Y. M.; He, J. H.; Tan, H. H.; Jagadish, C.; Catchpole, K. Over 17% Efficiency Stand-Alone Solar Water Splitting Enabled by Perovskite-Silicon Tandem Absorbers. *Adv. Energy Mater.* **2020**, No. 2000772.

(35) Lei, Z. Y.; Xu, S. J.; Wu, P. Y. Ultra-thin and Porous MoSe<sub>2</sub> Nanosheets: Facile Preparation and Enhanced Electrocatalytic Activity towards the Hydrogen Evolution Reaction. *Phys. Chem. Chem. Phys.* **2016**, *18*, 70–74.

(36) Gao, X. C.; Feng, J.; Su, D. W.; Ma, Y. C.; Wang, G. X.; Ma, H. Y.; Zhang, J. T. In-Situ Exfoliation of Porous Carbon Nitride Nanosheets for Enhanced Hydrogen Evolution. *Nano Energy* **2019**, *59*, 598–609.

(37) Hou, Y.; Qiu, M.; Kim, M. G.; Liu, P.; Nam, G.; Zhang, T.; Zhuang, X.; Yang, B.; Cho, J.; Chen, M. W.; Yuan, C.; Lei, L. C.; Feng, X. L. Atomically Dispersed Nickel-Nitrogen-Sulfur Species

Anchored on Porous Carbon Nanosheets for Efficient Water Oxidation. *Nat. Commun.* **2019**, *10*, No. 1392.

(38) Wang, Z. W.; Lia, X. L.; Tan, C. K.; Qian, C.; Grimsdale, A. C.; Tok, A. L. Y. Highly Porous SnO<sub>2</sub> Nanosheet Arrays Sandwiched within TiO<sub>2</sub> and CdS Quantum Dots for Efficient Photoelectrochemical Water Splitting. *Appl. Surf. Sci.* **2019**, *470*, 800–806.